Magnetic Resonance Imaging 61 (2019) 187–195

Contents lists available at ScienceDirect

Magnetic Resonance Imaging

journal homepage: www.elsevier.com/locate/mri

Original contribution

Shape-appearance constrained segmentation and separation of vein and artery in pulsatile tinnitus patients based on MR angiography and flow MRI

Yan Wang[a], Evan Kao[a], Yue Zhang[b,c], Bing Tian[d,*], Jingshan Gong[e], Farshid Faraji[a], Henrik Haraldsson[a], Matthew R. Amans[a], David Saloner[a,c], Jing Liu[a]

[a] Department of Radiology and Biomedical Imaging, University of California San Francisco, CA, United States
[b] Department of Surgery, University of California San Francisco, CA, United States
[c] Veteran Affairs Medical Center, San Francisco, CA, United States
[d] Department of Radiology, Changhai Hospital of Shanghai, Shanghai, China
[e] Department of Radiology, Shenzhen People's Hospital, Shenzhen, China

ABSTRACT

This study reports on the development and evaluation of a novel segmentation method for extracting the internal jugular vein and the adjacent carotid artery from magnetic resonance (MR) images of patients with pulsatile tinnitus. A narrow band level set method with combined shape and appearance constraints was developed and applied to high-resolution MR images from 17 pulsatile tinnitus patients (age 52 ± 23 years, 10 females). The proposed method was validated by comparing with the manual segmentation as well as by identifying the jugular vein and carotid artery based on 4D flow MRI in which the two types of vessels have opposing flow. Our study showed that the vein and artery are in contact with each other on 30.2% of all the slices. Dice value, Peak signal-to-noise ratio (PSNR), Hausdorff distance and mean sum of square distance (MSSD) between automatic and manual segmentation were 89.13 ± 2.84%, 27.36 ± 2.39%, 17.2 ± 6.9 mm, 7.4 ± 5.5 mm, demonstrating good segmentation accuracy. The average Dice similarity coefficient and the coefficient of variation compared with 4D flow MRI was 91.42 ± 1.63% and 89.28 ± 4.54% for the internal jugular vein and the carotid artery. The present pipeline for automatic internal jugular vein quantification holds promise for efficient image interpretation in large-scale cohort studies.

1. Introduction

Tinnitus affects > 50 million people in Unite States, and it is the auditory perception of sound in the absence of an external source [1]. A subset of these cases (5–10%) is attributable to pulsatile tinnitus (PT) which involves the sensation of hearing a rhythmic swooshing or whooshing [2,3] that is synchronized with the cardiac pulse. PT severely reduces the quality of life - nearly 60% of the patients who experience PT suffer related depression or anxiety [1].

PT is regularly related to abnormal flow in vessel structures near the cochlea [1,4]. One vessel territory occupied in PT is the internal jugular vein (IJV). PT etiologies can be venous (40%), arterial (35%), or undetermined (25%) [5]. MRA is a powerful technique to assess the geometric features of vessels. It is most commonly applied for imaging arteries but can also be used for veins. Segmentation of the artery and vein in MRA is key point for detecting and quantitative measurement of PT disease. However, arteries and veins are often adjacent, touching, or even draped over one another, in certain locations. These types of configurations represent a significant challenge in separating arteries from veins.

A number of studies have investigated the anatomic relationship of the IJV to the carotid artery (CA) [6–10] using manual delineation of the IJV and CA on two-dimensional (2D) ultrasound. This is time-consuming, technically demanding, and limited in capturing the tortuous 3D anatomy. Computer automated techniques to separate arteries and veins have also been investigated [11–16]. Charbonnier et al. presented a method for separation and classification of pulmonary arteries and veins in computed tomography using tree partitioning and peripheral vessel matching [11]. Lei et al. proposed a fuzzy connected object delineation principles and algorithms to separate artery-vein [13]. Payer et al. used integer programming to arteries and veins separation from thoracic CT [14]. An improved artery-vein separation method with acceleration-dependent preparation was proposed by Priest et al. [15]. All the studies mentioned above were targeted at artery-vein classification, and placed lower priority on getting accurate vessel geometry compared to manual segmentation. Karami et al. proposed a technique for IJV segmentation in ultrasound images using active contours [12], but they applied that to healthy subjects without vascular abnormalities. Computer-aided segmentation of the IJV and CA in MR images has not been previously attempted in patients with vascular abnormalities.

In this study, we developed an automated segmentation pipeline to determine the morphology and anatomic relationships of the IJV and

* Corresponding author at: Radiology, Changhai Hospital, 168 Changhai Road, Yangpu District, Shanghai, China.
E-mail address: bing.tian@hotmail.com (B. Tian).

https://doi.org/10.1016/j.mri.2019.05.026
Received 14 February 2019; Received in revised form 3 May 2019; Accepted 19 May 2019

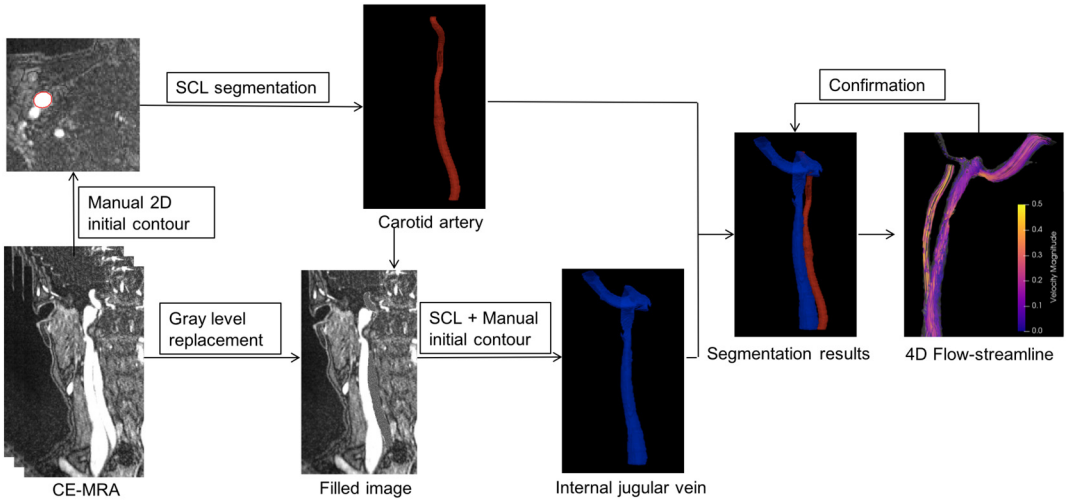

Fig. 1. IJV and CA segmentation scheme. The proposed segmentation scheme first uses the SCL method and a 2D manual initial contour to segment the CA from the CE-MRA images. The intensity values of the CA region are then replaced with the mean value outside it and the new image is marked as "filled". This operation blends the CA with the background. The SCL method and a 2D manual initial contour are then used to segment the IJV from the "filled image". Based on the segmented CA and IJV geometries, the 4D flow streamline is generated to confirm the segmentation results.

CA in PT patients based on MRI studies. We attempted to achieve accurate delineation even in the presence of touching vessels (artery and vein). The proposed approach is a shape-appearance constrained level set method (SCL), which adapts the level set equation for artery and vein separation by adding an elliptically refined term and a similarity term. The accuracy of SCL was validated compared with the conventional manual segmentation methods. However, even manual segmentation was particularly challenging in regions where the IJV and CA are in contact, and it was difficult to discern a boundary between the vessels. The proposed SCL method was further validated using 4D flow MRI data to confirm the separation of the vessels using the a priori knowledge that flow directionality is in opposite directions in arteries and veins.

2. Methods

2.1. MR acquisitions

Patients were recruited from the University of California San Francisco (UCSF) Medical Center Pulsatile Tinnitus Clinic and provided informed consent for participation in accordance with the procedures approved by our Institutional Review Board. Total 17 patients underwent a 3 T Siemens Skyra (Siemens Medical Systems, Erlangen, Germany) with a high-resolution contrast enhanced MR angiogram (CE-MRA) and phase-contrast MRI (PC-MRI) to define the geometric morphology and 4D flow velocity fields.

The 3D CE-MRA was obtained with isotropic resolution (0.7 mm) in the coronal plane with 45 s acquisition time. Other main MR parameters were: TR/TE = 3.66/1.4 ms, flip angle = 20°, FOV = 200 mm, image matrix = 320 × 240, and number of slices = 172.

The 4D flow MRI was also acquired on 7 of the 17 patients. The acquisition took about 10 mins and was reconstructed into images with a temporal resolution of 80 ms and total 9–12 cardiac phases depending on subject-specific heart rate. Other parameter settings include: FOV = 151 × 230 mm^2, isotropic resolution = 1.3 × 1.3 × 1.3 mm^3, flip angle = 8°, in-plane imaging matrix = 116 × 176, number of slices = 24–28, and TR/TE = 4/1.6 ms.

2.2. Study design

We proposed an SLC method to segment and separate the IJV from the CA. The SLC method has two important terms: one is the level set term, and the other one is the shape prior term. The level set term controls the implementation of a curve evaluation stop at the object boundary, and the shape prior term ensures that the final result to be similar to the prior. Thus the method allows to produce a reasonable estimate of the wall based on the shape prior, even when the wall is not clear between the IJV and the CA.

The study includes four main steps. The first step was the automatic segmentation and separation of CA and IJV using the SLC method. The IJV and CA diameters have different ranges (from 9.1 mm to 10.2 mm and from 4.3 mm to 7.7 mm, respectively). We first segment the smaller vessel (CA) using the proposed SLC method. The second step was the manual segmentation on the same patients' data and the comparison between automatic and manual segmentation to assess segmentation accuracy. The third step was the use of 4D flow MRI to separate the CA and IJV followed by a comparison of the contours defined by flow direction with the boundaries determined by the automatic segmentation. The final step was quantitative measurements of metrics of geometric morphology performed on the segmented vessels.

2.3. Segmentation methodology

The proposed segmentation scheme first uses the SCL method to segment the CA from the CE-MRA images. The intensity values of the CA region are then replaced with the mean value outside it and the new image is marked as a "filled" image. This operation blends the CA with the background. SCL method is then used to segment the IJV from the "filled" images. For the entire 3D image segmentation, SCL requires only one manual initial contour on a 2D slice. After that, the method automatically detects the contour in subsequent slices, using the result from the previous slice as a reference. The segmentation scheme is shown in Fig. 1.

2.4. Shape-appearance constrained level set (SCL)

Since we are considering the vascular structure, which is bounded by an ellipse-like contour, we use SCL method to separate the IJV and CA. In the present study, the energy formulation can be modified as follows based on the classic level set method:

$$E = E_{level\ set} + \alpha E_{ellipse} + \beta E_{similarity}, \quad (1)$$

where $E_{level\ set}$ represents the classic level set term, $E_{ellipse}$ represents the ellipse-like shape prior, and $E_{similarity}$ embeds the shape term. α and β

are weight of each term, which correspond to positive hyper-parameters that balance the impact between these three terms. As Alessandrini et al. pointed out [17], $E_{level\ set}$ could be any of the data attachment terms, and we adopt the narrow band level set as the data attachment term. The level set equation is generated by minimizing the energy function $E_{level\ set}$ with respect to ϕ:

$$\frac{\partial \phi(x,t)}{\partial t} = f(x)\delta(\phi(x,t)) \tag{2}$$

where $f(x)$ is given by:

$$f(x) = \int B(x,y)\delta(\phi(y))[(I(y)-u_x)^2 - (I(y)-v_x)^2]dy, \tag{3}$$

$$B(x,y) = \begin{cases} 1 & if\ y \in N_B(x) \\ 0 & otherwise \end{cases}, \tag{4}$$

where y is a spatial variable in a defined neighborhood $N_B(x)$ by user. The quantities u_x and v_x correspond to the average gray levels measured both inside and outside the region of $N_B(x)$, respectively.

$E_{ellipse}$ embeds the ellipse-like shape prior term which is defined by minimizing the following energy function:

$$E_{ellipse}(\phi,\ \lambda) = \int (\phi(x) - \phi_e(x,\ \lambda))^2\delta(\phi(x))dx, \tag{5}$$

$$\phi_e(x,\ \lambda) = \frac{F(x,\ \lambda)}{|\nabla F(x,\ \lambda)|}, \tag{6}$$

$$F(x,\ \lambda) = \lambda_1 x_1^2 + \lambda_2 x_1 x_2 + \lambda_3 x_2^2 + \lambda_4 x_1 + \lambda_5 x_2 + \lambda_6 \qquad with\ \ \lambda_2 < 4\lambda_1\lambda_3 \tag{7}$$

where $\phi_e(x)$ represents the Sampson distance [18], which is the first order approximation of the geometric distance of a point x from the annular shape determined by the parameter λ [17], and $F(x,\ \lambda)$ corresponds to the algebraic distance of a point $x = (x_1,\ x_2)$ to an ellipse, calculated with the standard quadratic equation for conic sections.

$E_{similarity}$ represents the shape term which is integrated in the energy function and measures the non-overlapping areas between the prior shape and the evolving level set shape. $\phi_i(x)$ and $\phi(x)$ denote the distance function of the prior shape and the evolving shape representation. This energy function is as follows:

$$E_{similarity} = \int (\phi(x) - \phi_i(x))^2 H(\phi(x))dx \tag{8}$$

where H is the Heaviside function.

2.4.1. Gray level replacement

The first application of the SCL segments the arterial region. In order to separate the artery from the abutting vein, the gray level value of the artery is replaced by the mean intensity of the region outside it. For each pixel inside of this region, the new intensity is defined as follows

$$I_{new} = \frac{\sum a_i}{n} + \varepsilon R \quad i \in [1,n] \tag{9}$$

where I_{new} represents the filled intensity from the artery region, a_i represents the intensity for each pixel outside the artery region, n is the number of pixel, ε is an infinitesimally small number and R is the added random noise.

2.5. Segmentation parameter setting

α and β are the only two parameters in the SCL segmentation, and are the weight of the ellipse term and the similarity term. In regard to the choice of the value of these two parameters: When α and β are low, for example, the extreme case of α = 0 and β = 0, corresponds to using the traditional level set segmentation. When α is high, the segmentation contour will be closer to an ellipse. In the extreme case α = 1, predominant weighting is given to the ellipse shape. Even under this condition, the contour cannot be 100% elliptical because the classic level set term in Eq. (1) also constrains the final result. For intermediate alpha values, local variations of the final contour will be closer to those of actual contours. β is the weight of the similarity term, which has lower weight compared to the ellipse term. In all the experiments segmentation of CA was first obtained by setting α and β to be 0.6 and 0.2, respectively. Then CA was replaced, and IJV was segmented using lower weights for the shape prior term, where α and β were set at 0.1 and 0.2.

Random noise was added in Eq. (9), set to 15% of the mean value of the region. The definition of ε is given as $\varepsilon = \frac{\sum b_i}{n} \times 15\%$.

2.6. 4D Flow MRI

4D Flow MR are similar to computational fluid dynamics simulation [19–24], which can show the velocity and flow information. In this study, 4D Flow MR images were used as a second method of validation for the IJV and CA segmentations. The direction of flow in pixels masked by the segmentation should indicate whether the segmentation is successful. Blood in pixels assigned to the IJV should flow caudally (towards the feet), while blood in pixels assigned to the CA should flow cranially.

4D MR images were processed using in-house Python tools. Background correction was performed to compensate for eddy-current-induced phase offset errors. The segmentations, which were derived from the CE-MRA image, were then registered to the 4D Flow images using Geomagic and Paraview. Quantitative analysis of segmentation accuracy based on the axial slice velocity direction was calculated in MATLAB (see Evaluation criteria). 2D slice visualizations were performed with Matplotlib, while 3D visualizations were performed in Paraview.

2.7. Evaluation criteria

2.7.1. Traditional segmentation matching factors

The proposed SCL method were evaluated by comparing the automatic segmentation results with the reference standard and 4D flow velocity using different criteria. Traditional segmentation matching factors such as Dice value, Peak signal-to-noise ratio (PSNR), Hausdorff distance, and mean sum of square distance (MSSD) were calculated in the present study to measure the overlap, distortion and distance between reference standard and automatic segmentation.

PSNR is a performance evaluation parameter that represents region homogeneity of the final partitioning, and can be used in evaluation of the image segmentation quality. The greater the Dice and PSNR values, the better the agreement between reference standard and automatic segmentation. The definition of Dice and PSNR values are as follows:

$$Dice\% = \frac{2\ |A \cap B|}{|A| + |B|} \times 100\%, \tag{10}$$

$$PSNR = 10log_{10}\left(\frac{d}{MSE(A,B)}\right), \tag{11}$$

$$MSE(A,B) = \frac{1}{MN}\sum_{m=1}^{M}\sum_{n=1}^{N}\|A(m,n) - B(m,n)\|^2. \tag{12}$$

where A is the automatic segmentation and B is the reference standard. || denotes the number of pixels in the corresponding volume.

The Hausdorff and MSSD are the distance between reference standard and automatic segmentation results. The Hausdorff distance measures how far two subsets of a metric space are from each other, and MSSD is the mean of the Euclidean distances between every vertex on one surface and its nearest neighboring vertex on the other surface. These two distances are defined as follows:

$$\text{Hausdorff} = \max(D_1(A,B),\ D_1(B,A)), \tag{13}$$

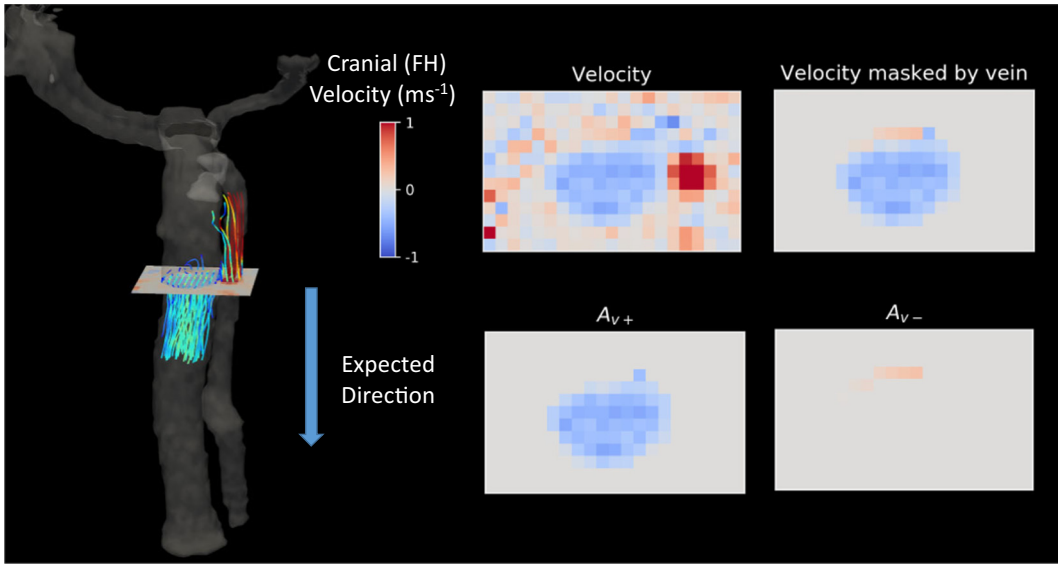

Fig. 2. A visual depiction of the velocity matching factor (VMF) criterion as applied to the venous segmentation. Velocities towards the head are encoded in red and towards the feet in blue. a. Blood flow in the jugular is generally directed towards the feet, which is taken to be the "expected direction"; b. The velocity map through one slice that includes both the IJV and CCA; c. The velocity map masked by the venous segmentation, showing both "arterial" and "venous" components; d. The set of voxels associated with the jugular vein (blue or negative, towards the feet) - excluding voxels with velocity directed in the incorrect direction (red or positive, towards the head); e. The set of voxels with velocity directed in the incorrect direction (red or positive, towards the brain). Together, d and e are used to calculate VMF. (For interpretation of the references to color in this figure legend, the reader is referred to the web version of this article.)

Table 1
Dice coefficients achieved with manual initial contours at different slice locations.

Dice (%)	CA segmentation	IJV segmentation
Slice no. 20	100	100
40	99.29	100
60	99.64	99.98
80	99.72	99.97
100	99.54	99.88
120	99.18	99.51
140	98.97	99.70
180	98.79	99.96
200	98.39	99.98
Mean ± std	99.28 ± 0.5	99.88 ± 0.17

$$D_1(A,B) = max_{x\in A}(min_{y\in B}(\|x-y\|y)); \tag{14}$$

$$MSSD = \frac{1}{N}\sum_{n=1}^{N} D_2^2(A,B(x_n)), \tag{15}$$

$$D_2(A,B(x)) = min_{y\in A}(\|y-x\|), \tag{16}$$

where N is the size of the result. The lower the Hausdorff and MSSD, the better the segmentation result.

2.8. Velocity matching factor

From 4D flow MRI, the distribution of the velocity component in the inferior-superior axis was extracted and compared to the automatic segmentation results using the "velocity matching factor" (VMF), which is defined as follows (Fig. 2):

$$VMF = \frac{V_A}{V_A + V_B}, \tag{17}$$

where V_A and V_B are the number of pixels which have the correct and incorrect velocity directions (generated from 4D flow data) inside the geometries obtained from SCL method. The greater the VMF value, the better the segmentation result. 1 indicates perfect overlap with 4D flow data, and 0 means no overlap.

In this study, 4D flow images have lower spatial resolution than CE-MRA (1.3∗1.3∗1.3 mm vs 0.7∗0.7∗0.7 mm). To make it feasible to combine 4D flow images for differentiating the vein and artery, we used a linear model to down sample the CE-MRA segmentation results to match the spatial resolution of 4D flow MRI before evaluating velocity directions.

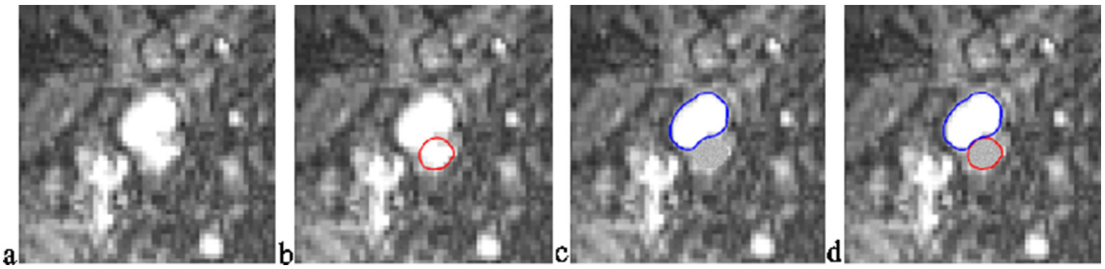

Fig. 3. A 2D slice from CE-MRA; b. artery segmentation contour obtained using SCL method; c. artery region replaced in "filled image"; d. the artery and vein segmentation results.

Table 2
Comparison of segmentation accuracy between the proposed SCL method and manual segmentation using 1) Dice value, 2) PSNR, 3) Hausdorff, and 4) MSSD.

Patient no.	Dice (%)	PSNR	Hausdorff (cm)	MSSD (cm)
1	87.97	25.41	1.92	1.53
2	85.06	22.53	1.65	0.70
3	84.74	24.82	0.86	0.22
4	93.14	28.67	1.62	0.68
5	90.44	29.53	2.17	0.77
6	92.33	27.10	1.60	0.37
7	87.70	28.11	2.20	0.48
8	86.02	22.76	1.84	0.51
9	91.90	28.69	0.50	0.16
10	81.04	29.85	0.41	0.22
11	90.93	27.40	1.64	0.53
12	90.45	25.30	2.95	2.19
13	88.65	28.95	1.18	0.23
14	86.42	27.97	2.73	1.03
15	92.44	29.83	2.41	0.57
16	91.85	30.23	1.89	1.05
17	87.94	28.08	1.78	1.42
Mean ± std	89.13 ± 2.84	27.36 ± 2.39	1.72 ± 0.69	0.74 ± 0.55

3. Experiment and results

3.1. Repeatability and reproducibility

A 2D manual initial contour was chosen at random and used in the present study, which may potentially influence the final segmentation results. The repeatability and reproducibility coefficients were computed from the standard deviation of the differences between the results made with different 2D manual initial contours for CA and IJV segmentation, respectively.

We chose 9 different slices (with slice number from 20 to 200, and 20 slice intervals) to draw initial contours for CA and IJV segmentation. The Dice value is shown in Table 1. The average Dice and standard deviation for these different contours are 99.28 ± 0.50% (CA) and 99.88 ± 0.17% (IJV), respectively. This demonstrates that the SCL segmentation has good repeatability and reproducibility.

3.2. Results

Our readers used a MeVisLab-based tool (http://www.mevislab.de/) to draw manual contours. In the present study, two readers reached consensus on the definition of contours by drawing manual contour for all the 2D slices of 5 patients. The inter-observer variability was 5.16 ± 2.82% and 5.53 ± 3.16% for IJV and CA, respectively. One radiologist subsequently drew manual contours for each slice of all the PT patients (17 subjects in total). Each PT patient had more than one hundred slices, and in total all patients had nearly two thousand slices. The radiologist also drew the manual contours two times for 5 PT patients. The intra-observer variability was 3.53 ± 3.47% and 4.18 ± 3.82% for IJV and CA, respectively.

The MRI images of IJV and CA of a representative case are shown in Fig. 3a. In many of the slices, there is no clear border between IJV and CA, so segmenting the vessels is challenging even for a highly-trained

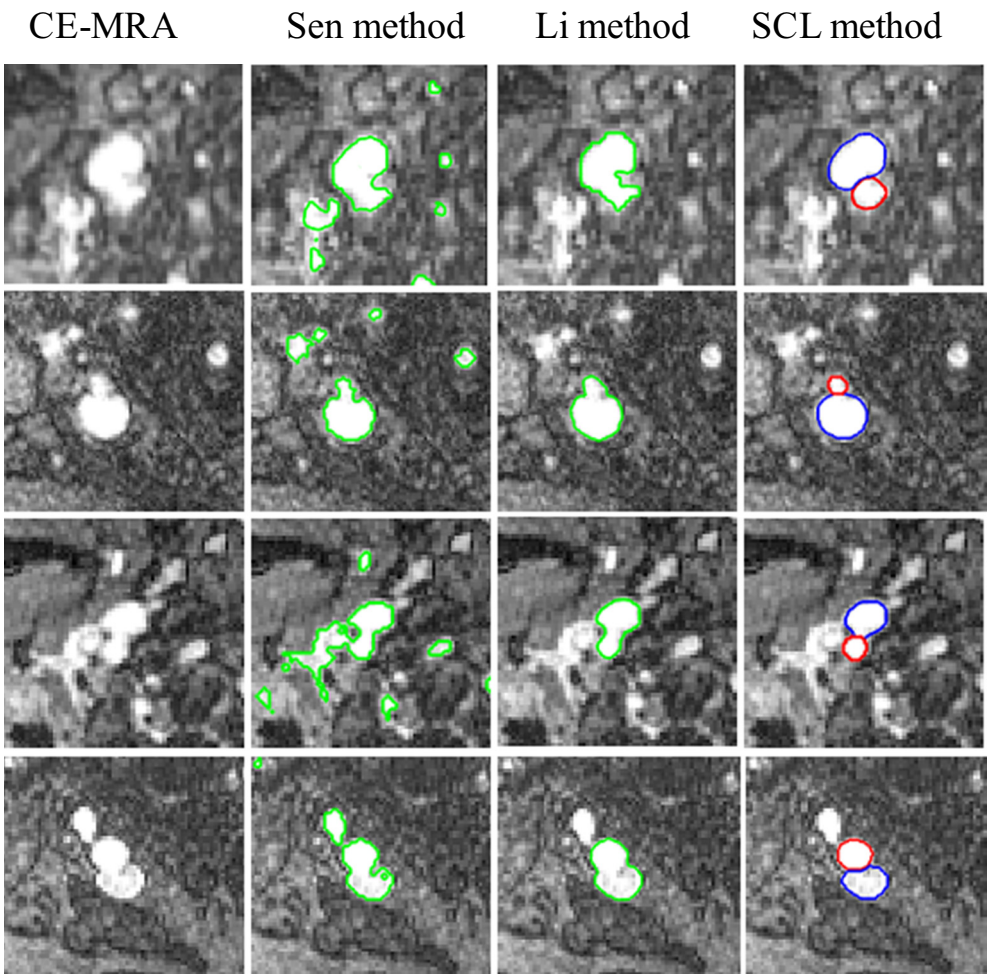

Fig. 4. The first column shows the CE-MRA images from four representative cases; the segmentation results from Sen method, Li method and the proposed SCL method are shown.

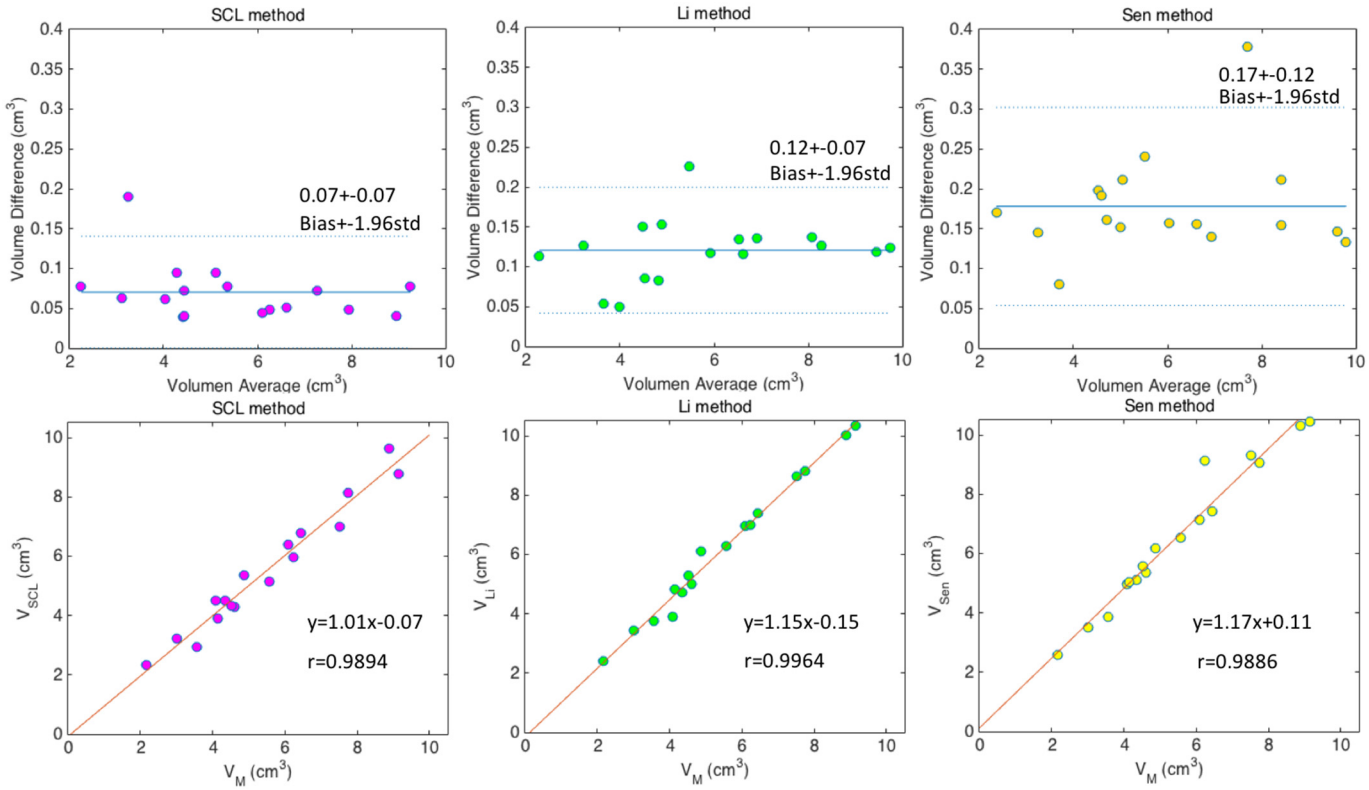

Fig. 5. Bland-Altman and linear regression plots of the volume measurements of IJV between manual and automatic segmentation. Three automatic segmentation are segmented and compared: SCL method, Li method and Sen method.

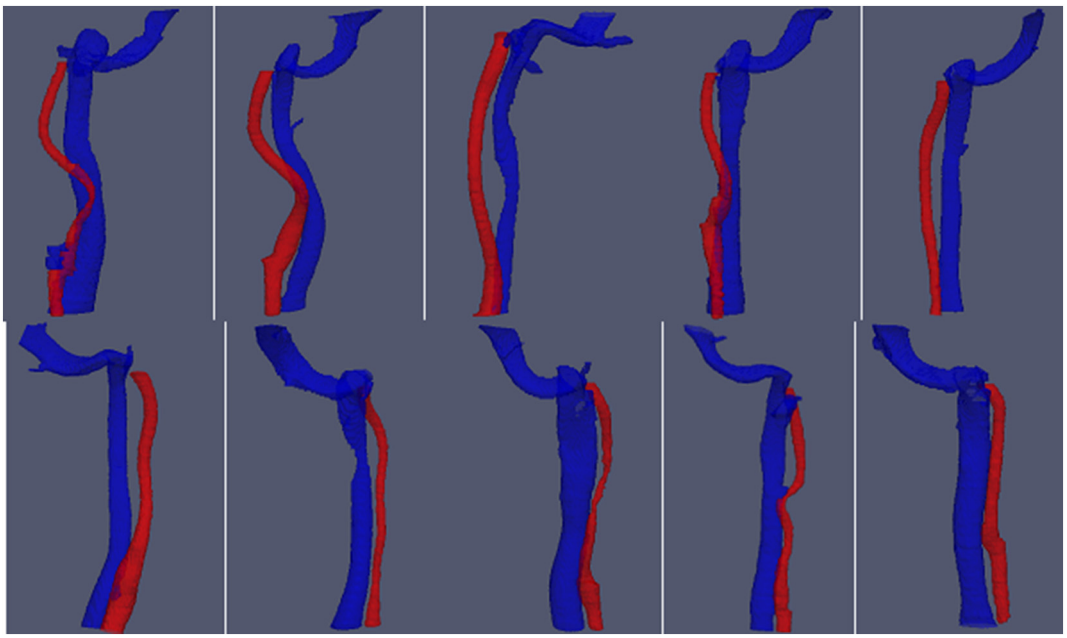

Fig. 6. Images from 17 patients were segmented in this study. 10 of the 17 reconstructed segmented geometries of the IJV (blue) and the CA (red) are shown here. (For interpretation of the references to color in this figure legend, the reader is referred to the web version of this article.)

radiologist. The intermediate results were shown in Fig. 3(b–d). The contour of the artery was first obtained after applying SCL, as shown in Fig. 3b; the region covering the artery in the MR images was then filled with a gray level replacement (Fig. 3c), thereby differentiating signals from the artery and vein. The venous contour was then determined by applying SCL method on the modified ("filled") images (Fig. 3d).

We applied the previously outlined SCL method to the 17 PT cases. Both the IJV and CA were successfully segmented and the results were comparable to the manual delineation. For quantitative comparison, the Dice value, PSNR, Hausdorff and MSSD are 89.13 ± 2.84%, 27.36 ± 2.39%, 17.2 ± 6.9 mm and 7.4 ± 5.5 mm (Table 2), respectively, which demonstrates that the proposed method achieved comparable and robust segmentation in comparison to the manual segmentation on multiple patients. An experienced radiologist took

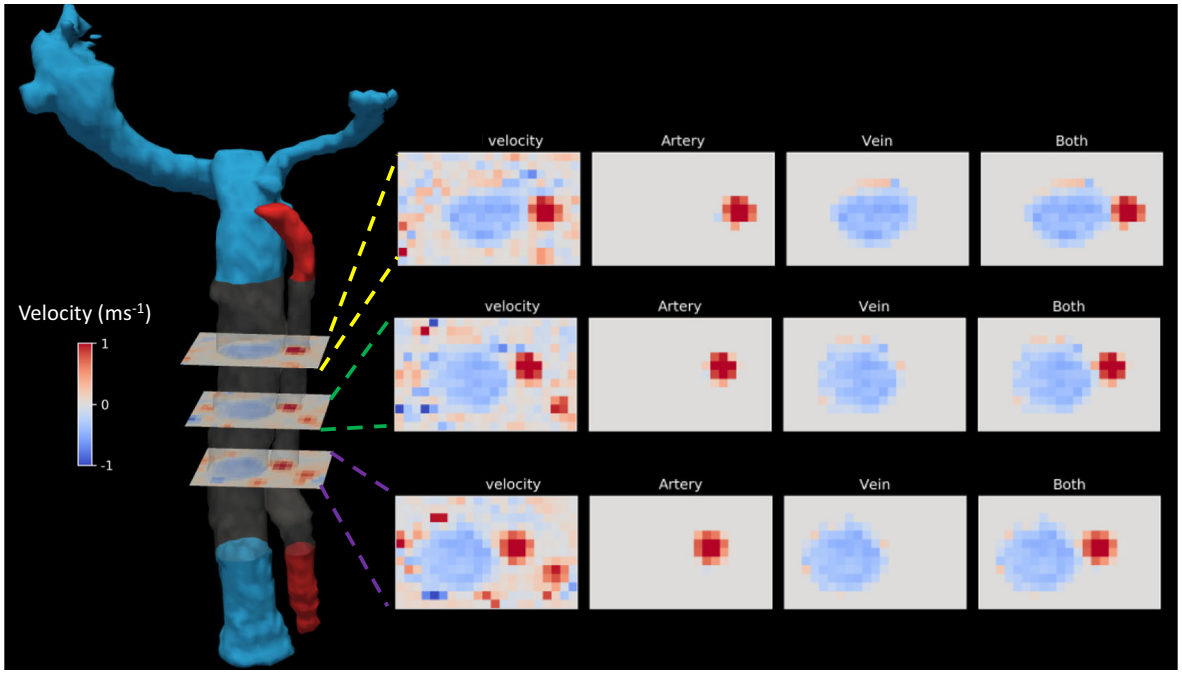

Fig. 7. A segmentation result of the IJV and CCA compared to its cranial velocity map for one case, illustrating the effectiveness of SCL method in segmenting the two vessels separately at regions of contact between them. The cranial velocity map is provided for three slices, as well as the velocity maps masked by the arterial and venous segmentations.

Table 3
Velocity matching factors measured for IJV and CA from 7 patients who also underwent 4D flow MRI were assessed to evaluate the segmentation accuracy.

Patient no.	IJV (%)	CA (%)
1	89.22	83.81
2	90.71	92.33
3	91.93	92.14
4	90.62	92.82
5	90.81	94.22
6	92.36	84.69
7	94.35	84.97
Mean ± std	91.42 ± 1.63	89.28 ± 4.54

Table 4
Quantitative measurements.

Patient no.	IJV volume (ml)	CA volume (ml)	Connection length (cm)	Stenosis (cm)
1	8.90	1.61	4.34	0
2	4.86	2.48	3.29	0
3	4.08	3.22	2.94	0
4	4.34	2.02	6.02	0.14
5	4.15	0.98	0	0.70
6	9.14	1.47	3.29	0
7	4.61	2.64	3.08	0
8	7.53	2.89	2.87	0
9	4.52	1.17	3.43	0
10	2.16	1.97	0.35	0
11	6.10	2.30	4.76	0
12	7.76	1.80	3.29	0
13	3.02	2.74	0.56	0
14	3.55	1.50	2.10	0
15	6.24	2.00	4.90	0
16	6.45	2.28	3.08	0
17	5.57	1.76	2.03	0

about 40 s to segment one slice, while the proposed method achieved comparable contours in < 10 s per slice (on a 2.2 GHz Intel laptop with 8GB RAM).

Fig. 4 shows the segmentations that were obtained with the reference Sen method [25], Li method [26], and the proposed SCL method. Compared to the manual segmentation, the Dice value for Sen method, Li method and the proposed SCL method are 62.00 ± 6.78%, 73.32 ± 6.15, and 89.13 ± 2.84% respectively. The volume measurements and difference between automatic and manual segmentations were compared. The Bland-Altman and the linear regression plots of IJV volume measurements were generated in Fig. 5. The correlation coefficients, linear fitting slope and offsets, mean bias and confidence intervals (± 1.96std) were calculated and reported in Fig. 5 comparing three automatic segmentation methods. As shown in Fig. 5, the proposed SCL method outperformed the Li and Sen methods, achieving best correlation and fitting, and a P value of 0.88 (*t*-test, not significantly different with 0.05 threshold) versus P < 0.01 for Li and Sen methods.

Fig. 6 provides ten different orientations of the 3D volume rendering visualization of the segmentation of the IJV and CA using the SCL method. The vessels are clearly separated even though they are touch in multiple locations.

As highlighted previously, efficiently and accurately identifying the ambiguous borders of the CA and the IJV is one of the main strengths of the proposed method compared to evaluation by a skilled reader. However, as noted earlier, separation of the touching vessels is challenging even for experienced radiologists. To confirm that the CA and IJV were segmented correctly, further evaluation based on the 4D flow MRI of the vessels was performed since blood flows in opposite directions in the two vessels of interest (shown in Fig. 7). By separating the pixels according to the velocity direction, we can verify that our SCL based contours are concordant with those of the CA and IJV. The VMF values between the automatic segmentation and the segmentation obtained using 4D flow images was high with values of 91.42 ± 1.63% and 89.28 ± 4.54% for IJV and CA, respectively (shown in Table 3).

Relevant clinical measurements such as the volume, the stenosis, and the connection length for the IJV and CA are summarized in Table 4. The quantitative measurements show that the length of the kissing vessels could be up to 1/4 of the length of the vessels, indicating that properly segmenting and separating the vessels is essential for

accurate clinical evaluation.

4. Discussion

Since the geometry of the blood vessels directly contributes to features in the blood flow, accurate geometric characterization of the involved vessels (including the internal jugular vein (IJV) and carotid artery (CA)) is extremely important in the clinical evaluation of patients [2,5]. The segmentation of the IJV and CA permits quantitative measurements of geometric characteristics, including regions of stenosis and volumetric measures, which are important parameters for clinical decision-making [5].

In the present study, we proposed a new segmentation method SCL to separate the IJV and CA in PT patients. SCL method was developed to address the following problem: estimate a vessel geometry with a partial contour by adding an elliptically-refined term and a similarity term to the level set energy formulation. The level set energy formulation was used to control the main segmentation contour based on the image gradient, while the elliptically-refined term and similarity terms are used to contour the segmentation similar to the reference contour and an ellipse. The latter two terms are the main components for estimating the missing contour.

There are two approaches for separating the artery and vein: mid-imaging and post-imaging. The mid-imaging technique relies on the difference in contrast agent uptake between the vessels [15,27]. However, the present study is a post-imaging image processing technique, which can not only separate the vein and artery, but can also be used on any touching vessels, e.g., the touching cerebral/internal carotid arteries in transverse view.

Manual segmentation was used as reference standard in a number of studies [28–33]. However, in our region of interest, our main concern is the lack of intra- and inter-observer repeatability of the contours given the absence of a clear boundary between the IJV and CA in the MR angiogram. In this study, we proposed to use 4D flow data to validate our segmentation results. The adjacent IJV and CA vessels have opposite blood flow directions. Therefore, 4D flow is helpful in determining which voxels in the angiogram belong to the artery or the vein.

All the segmentations were validated by manual segmentation. Dice value, PSNR, Hausdorff and MSSD between automatic and manual segmentation were 89.13 ± 2.84%, 27.36 ± 2.39%, 17.2 ± 6.9 mm and 7.4 ± 5.5 mm, which demonstrate good segmentation accuracy. The results showed that the SCL method provided comparable segmentation compared to the manual segmentation. It also provided better accuracy than two other previously proposed methods. Seven patient studies were validated using 4D flow and the VMF was 91.42 ± 1.63%. We note that the 4D flow validation result is comparable with the manual validation, which has a similar matching value. The two main limitations for manual delineation are that it is time consuming and has poor reproducibility. Since comparison with 4D flow MRI requires relatively little additional manual work, it is potentially a more efficient method of validation.

This study still has some limitations. First, a manual initial contour was used for jugular segmentation. In future studies, we will further explore the feasibility of providing an accurate automatic initial contour regardless of the vessel geometry. Second, the 4D flow is noisy, and that can play a substantial role in our validation accuracy. We have used a median filter to denoise 4D flow images. In future studies, we would like to improve denoising methods to achieve better results. Third, incorporating a 4D flow related term to the segmentation method would be valuable not only for refining the segmentation but also for differentiating vein and artery depending on the flow directions. However, there are some challenges that make it difficult to combine both MRA and 4D flow MRI data in the algorithm. The main challenge is that 4D flow MRI has much lower spatial resolution than CE-MRA. To match the data, up sampling 4D flow images or down sampling the CE-MRA is required, which can cause significant errors in the input data and consequently in the steps in the segmentation algorithm. In this study, we processed the two types of images under the same resolution (the lower one). Due to larger voxel size, the partial volume effect in 4D flow images, does cause signal loss and affect the velocity accuracy. Ideally we like to get higher spatial resolution 4D flow MRI to reduce the partial volume effect. Also, higher spatial resolution 4D flow MRI is desirable to make it feasible to add a 4D flow related term into the segmentation method.

In future studies, 4D flow could be used to refine the segmentation results in the following two ways: 1) 4D flow MRI can be used to correct the small errors near the borders that were obtained when using the SCL method; 2) A new term including 4D flow data could be added to the level set formula. This term could assign negative and positive numbers for vein and artery, respectively, in order to accurately define and separate the vessels. To achieve those, a highly accelerated technique is needed to reduce the scan time and increase the spatial resolution of 4D flow imaging.

In the present study, a reliable and reproducible pipeline for automatic quantification of geometric metrics of the internal jugular vein was developed and validated on patient-specific pulsatile tinnitus subjects. This method holds promise for helping in efficient image interpretation for large-scale cohort studies.

Acknowledgements

This work was supported in part by grant from the NIH R21DC016087 (MA), R01HL114118 (DS) and R56HL133663 (JL).

Declaration of Competing Interest

The authors declare that they have no competing interests.

References

[1] Krishnan A, Mattox DE, Fountain AJ, Hudgins PA. CT arteriography and venography in pulsatile tinnitus: preliminary results. AJNR Am J Neuroradiol 2006;27(8):1635–8.
[2] Harvey RS, Hertzano R, Kelman SE, Eisenman DJ. Pulse-synchronous tinnitus and sigmoid sinus wall anomalies: descriptive epidemiology and the idiopathic intracranial hypertension patient population. Otol Neurotol 2014;35(1):7–15.
[3] Liyanage S, Singh A, Savundra P, Kalan A. Pulsatile tinnitus. J Laryngol Otol 2006;120(02):93–7.
[4] Madani G, Connor S. Imaging in pulsatile tinnitus. Clin Radiol 2009;64(3):319–28.
[5] Mattox DE, Hudgins P. Algorithm for evaluation of pulsatile tinnitus. Acta Otolaryngol 2008;128(4):427–31.
[6] Miki I, Murata S, Nakazawa K, et al. Anatomical relationship between the common carotid artery and the internal jugular vein during head rotation. Ultrasound 2014;22(2):99–103.
[7] Podgórski M, Winnicka M, Polguj M, Grzelak P, Łukaszewski M, Stefańczyk L. Does the internal jugular vein affect the elasticity of the common carotid artery? Cardiovasc Ultrasound 2016;14(1):40.
[8] Qin X-h, Zhang H, Mi W-d. Anatomic relationship of the internal jugular vein and the common carotid artery in Chinese people. Chin Med J (Engl) 2010;123(22):3226–30.
[9] Shoja MM, Ardalan MR, Tubbs RS, et al. The relationship between the internal jugular vein and common carotid artery in the carotid sheath: the effects of age, gender and side. Ann Anat 2008;190(4):339–43.
[10] So KY, Kim SH, Kim DW. Anatomical relationship of the internal jugular vein and the common carotid artery in Korean: a computed tomographic evaluation. Anesthesia and Pain Medicine 2015;10(2):118–23.
[11] Charbonnier J-P, Brink M, Ciompi F, Scholten ET, Schaefer-Prokop CM, van Rikxoort EM. Automatic pulmonary artery-vein separation and classification in computed tomography using tree partitioning and peripheral vessel matching. IEEE Trans Med Imaging 2016;35(3):882–92.
[12] Karami E, Shehata M, McGuire P, Smith A. A semi-automated technique for internal jugular vein segmentation in ultrasound images using active contours. Biomedical and Health Informatics (BHI), 2016 IEEE-EMBS International Conference on. IEEE; 2016. p. 184–7.
[13] Lei T, Udupa JK, Saha PK, Odhner D. Artery-vein separation via MRA-an image processing approach. IEEE Trans Med Imaging 2001;20(8):689–703.
[14] Payer C, Pienn M, Bálint Z, Olschewski A, Olschewski H, Urschler M. Automatic artery-vein separation from thoracic CT images using integer programming. International Conference on Medical Image Computing and Computer-Assisted Intervention. Springer; 2015. p. 36–43.
[15] Priest AN, Taviani V, Graves MJ, Lomas DJ. Improved artery–vein separation with

acceleration-dependent preparation for non–contrast-enhanced magnetic resonance angiography. Magn Reson Med 2014;72(3):699–706.
[16] van Bemmel CM, Spreeuwers LJ, Viergever MA, Niessen WJ. Level-set-based artery-vein separation in blood pool agent CE-MR angiograms. IEEE Trans Med Imaging 2003;22(10):1224–34.
[17] Alessandrini M, Dietenbeck T, Basset O, Friboulet D, Bernard O. Using a geometric formulation of annular-like shape priors for constraining variational level-sets. Pattern Recogn Lett 2011;32(9):1240–9.
[18] Szpak ZL, Chojnacki W, Van Den Hengel A. Guaranteed ellipse fitting with the sampson distance. European Conference on Computer Vision. Berlin, Heidelberg: Springer; 2012, October. p. 87–100.
[19] Malaspinas, O., Turjman, A., de Sousa, D. R., Garcia-Cardena, G., Raes, M., Nguyen, P.T. et al., A spatio-temporal model for spontaneous thrombus formation in celebral aneurysms. J Theor Biol, 394, 68–76.
[20] Zhang Y, Wang Y, Kao E, Florez-Valencia L, Courbebaisse G. Towards optimal flow diverter porosity for the treatment of intracranial aneuysm. J Biomech 2019;82:20–7. Jan 3.
[21] Noel R, Ge F, Zhang Y, Navarro L, Courbebaisse G. Lattice Boltzmann method for modeling of biological phenomena. 2017 25th European Signal Processing Conference (EUSIPCO). IEEE; 2017 Aug 28. p. 2643–58.
[22] Zhang Y. Hemodynamic investigation and thrombosis modeling of intracranial aneurysms Diss Lyon: INSA; 2015.
[23] Xuan Y, Wang Z, Liu R, Haraldsson H, Hope MD, Saloner DA, et al. Wall stress on ascending thoracic aortic aneurysms with bicuspid compared with tricuspid aortic valve. J Thorac Cardiovasc Surg 2018;156(2):492–500. Aug 1.
[24] Wang Z, Wood NB, Xu XY. A viscoelastic fluid-structure interaction model for carotid arteries under pulsatile flow. Int J Numer Methods Biomed Eng May 2015;31(5):e02709.
[25] Sen Y, Qian Y, Avolio A, Morgan M. Image segmentation methods for intracranial aneurysm haemodynamic research. J Biomech 2014;47(5):1014–9.
[26] Li C, Xu C, Gui C, Fox MD. Distance regularized level set evolution and its application to image segmentation. IEEE Trans Image Process 2010;19(12):3243–54.
[27] Wang Y, Yu Y, Li D, Bae KT, Brown JJ, Lin W, et al. Artery and vein separation using susceptibility-dependent phase in contrast-enhanced MRA. J Magn Reson Imaging 2000;12(5):661–70.
[28] Wang Y, Courbebaisse G, Zhu Y-M. Segmentation of giant cerebral aneurysms using a multilevel object detection scheme based on lattice Boltzmann method. Signal processing, communications and computing. 2011. p. 1–4. IEEE International Conference on.
[29] Wang Y, Seguro F, Kao E, Zhang Y, Faraji F, Zhu C, et al. Segmentation of lumen and outer wall of abdominal aortic aneurysms from 3D black-blood MRI with registration based geodesic active contour model. Med Image Anal 2017;40(1):1–10.
[30] Chen Y, Navarro L, Wang Y, Courbebaisse G. Segmentation of the thrombus of giant intracranial aneurysms from CT angiography scans with lattice Boltzmann method. Med Image Anal 2014;18(1):1–8.
[31] Wang Y, Zhang Y, Navarro L, Eker OF, Corredor Jerez RA, Chen Y, et al. Multilevel segmentation of intracranial aneurysms in CT angiography images. Med Phys 2016;43(4):1777–86.
[32] Wang Y, Navarro L, Zhang Y, Kao E, Zhu Y, Courbebaisse G. Intracranial aneurysm phantom segmentation using a 4D lattice Boltzmann method. Comput Sci Eng 2017;19(4):56–67.
[33] Wang Y, Zhang Y, Xuan W, Kao E, Cao P, Tian B, et al. Fully automatic segmentation of 4D MRI for cardiac functional measurements. Med Phys 2019;46(1):180–9. Jan.